PROCEEDINGS, 47th Workshop on Geothermal Reservoir Engineering
Stanford University, Stanford, California, February 7-9, 2022
SGP-TR-223

# Observation of Meq HHz Coda in the Ambient Crust -- Implications for Surface Seismic Array Flow Imaging

Peter Leary and Peter Malin

Geoflow Imaging Ltd – peter@geoflowimaging.com

Advanced Seismic Instrumentation & Research – pem@asirseismic.com

**Keywords:** ambient crust; poroperm distributions; microseismicity; seismic scattering; coda waves; Arps decline curves; flow imaging

## ABSTRACT

We study the scattering of hectohertz (hHz) seismic emissions (f ~ 500 ± 200 Hz) from microseisms (Meqs) induced by fluids injected at 6km depth in crystalline basement as recorded by sensors 4km above the events. Some 90% of Meq hHz seismic emission energy is scattered into multi-second coda wavetrains with negligible intrinsic attenuation (Q ~ 3000). Coda amplitudes decline as hyperbolic function $H(t) \sim 1/(a+bt)^{1/b}$, $1 < b < 2$. Numerical 3D acoustic wave scattering replicates decline profiles with $1 < b < 2$ for "pink noise" spatially correlated wave speed fluctuations attested by well-log power-law scaling empirics; codas for higher/lower wave speed fluctuation correlation ("red/white noise") decline with $b \sim 1$; $b = 0$ gives exponential decline. Meq hHz waveform spectral modelling shows induced dislocation slip velocities to be slow/erratic along reactivated ambient crust poroperm structures; we note that these crustal flow structures are observed to drain according to hyperbolic well production decline timelines. Coda wave scattering thus links crustal reservoir Meq seismic emissions to reservoir flow activity. Using this link, long duration coda waves recorded at decaHz frequencies on surface seismic arrays above crustal reservoirs can be processed into signal energy stacks that map persistent Meq emission flow-connectivity structures in accordance with seismic imaging conducted at stimulated shale formations.

## 1. INTRODUCTION

Analysis of crustal seismic waves and seismic activity has long provided our most extensive understanding of the relation between crustal structures and the flow of crustal fluids. There remains, however, a fundamental wavelength disparity between what we want to know about crustal fluid flow and what standard processing of seismic waves and seismic activity tells us. Fluids interact with the crust across many decades of scale length – say from mm to km -- while typically seismic waves interact with the crust over a limited scale range of perhaps a decade -- say $50 < \lambda < 500$ m with geometric mean $\underline{\lambda} \sim 160$ m corresponding to decaHz frequencies $100 > f > 10$ Hz with geometric mean $\underline{f} \sim 30$ Hz.

The narrow range of seismic wavelength observation has meant historically that seismic data are taken as spatial averages over the many scales of fluid flow interest. Such spatial averaging has little statistical meaning unless the relevant crustal property spatial fluctuations are either weakly correlated or strongly correlated. Weak crustal spatial correlations can be treated as familiar uncorrelated Gaussian distributions, while strong spatial correlations can be treated as discrete structures bounded by step-function interfaces. Unfortunately for these stochastic approximations, actual crustal flow processes have a very definite intermediate degree of spatial correlation – neither weak nor strong – across the full range of crustal flow structure scale lengths. Discordance between standard model statistics and the statistics of actual crustal flow structures creates a persistent and serious barrier to using seismic data to understand the structure of crustal reservoir fluid flow systems.

We present a suite of reservoir-scale hectohertz (hHz) seismic waveform data with characteristic frequency $\underline{f} \sim 430$Hz, a full decade higher than standard reservoir-scale seismic data. The corresponding characteristic mean data wavelength is $\underline{\lambda} \sim 10$m. Our study waveforms arise from Meqs induced by controlled fluid injection into a km-scale crystalline basement stimulation volume at 6km depth [1]. The waveforms are recorded at 2kHz sampling rate by vector motion sensors at 2.5km depth directly above the stimulation volume. In the time/space of a 1s/4km source-to-sensor travel-path, seismic wave scattering is observed to transfer more than 90% of Meq emission energy out of the leading emission wavefront into multi-second-long trailing coda waves. The extended coda wave amplitude decay is purely elastic as given by hyperbolic decline $H(t) \sim 1/(a+ bt)^{1/b}$, $b > 1$ [e.g., 2], rather than inelastic decline as given by $E(t) \sim \exp(-t/a)$ [e.g., 3-5], where $E(t) \sim 1/(a+ bt)^{1/b}$ for $b \rightarrow 0$.

The observed hHz seismic emission wave scattering is notable on four grounds. First, the characteristic mean wavelength $\underline{\lambda} \sim 10$m does not conform to emissions from a standard planar fault structure as is routinely assumed for reservoir seismicity. Second, the extensive scattering of a mean wavelength $\underline{\lambda} \sim 10$ over 4000 meters travel paths cannot be logically treated as a standard "single scattering" process which leaves the primary wave essentially intact throughout the travel-path. Third, at $\underline{\lambda} \sim 10$ mean wavelength, the emission wavelets and their scattering coda wavetrain interact with crustal structures at scales an order of magnitude smaller than is standard for reservoir monitoring seismic data. Finally, both the amplitude decline of coda wavetrain spatial scattering and the decline of production well flow rates are described by hyperbolic functions rather than exponential functions. On these grounds, we can expect to interpret the hHz Meq field data in terms of spatial distributions of crustal property fluctuations embedded in the recorded wavefield and its coda wavetrain rather than as waves that average over uncorrelated and/or discrete crustal fluctuations. If hHz Meq waveform and scattering data are seen as embedded with crustal poroperm property spatial correlations that condition reservoir flow structures, we can widen our observational/interpretational approach to using seismic data to better manage reservoir flow.

The following discussion elaborates on the high frequency seismic waveform emission and scattering embeddedness theme to develop a picture of seismic wave interaction with spatially correlated poroperm structures for ambient crust reservoirs. Interaction of the $\underline{\lambda} \sim 10$ m scattering wavefield with crustal poroperm fluctuations of order $\ell \sim 100$ m can be data-processed into observations of crustal fluid-flow-induced seismic emission structures associated with active reservoir flow as is now routinely performed at shale formation stimulation production sites [6-10].

## 2. EMPIRICS OF SEISMIC DISLOCATION AND EMISSION WAVE SCATTERING IN THE AMBIENT CRUST

Our present picture of the material properties of ambient crustal rock and its fluid content contrasts fundamentally with existing standard reservoir formation approximations. As noted by two prominent contributors to these subjects, existing studies of crustal reservoir Meq waveforms and their possible crustal scattering are essentially defined by underlying observer assumptions rather than by first-order observations of ambient crustal media as developed here.

(1) Meq rock fracture processes are characteristically associated with fluid transmission by cubic-law flow along planar slip structures without anyone ever seeing Meq slip or slip structures:

> *Microseismicity occurs because of geomechanical changes to the reservoir as a result of the fracturing process, and detection and location of these "events" provides a methodology to monitor fracture growth patterns and overall dimensions. One of the curious features of microseismic technology is that no one has ever seen the slippage plane of a microseism that was induced by a hydraulic fracture. As a result, the understanding of microseismicity has been through a down-scaling of earthquake seismology... N Warpinski (2013) DOI: 10.5772/55974*

(2) Seismic wave scattering is historically expressed in terms of collections of individual scattering objects that almost exclusively involve incident wavefields that are assumed to remain unperturbed by the scatterers. The stochastic nature of the ambient crust scattering medium is rarely the starting point for the scattering formalism:

> *It has been well established that there is a strong link between the medium heterogeneity and the characteristics of seismogram envelopes; however, we note that there is not yet a wave theoretical method to derive coda attenuation $1/Q_C$ from the stochastic characterization of random media... H Sato & M Fehler (2009) DOI 10.1007/978-3-540-89623-4*

Our discussion is anchored by the elastic scattering of high frequency Meq emissions defined by Figures 1-2. These data place ambient crust Meq slip processes and spatial distributions of crustal poroperm properties in an empirical framework of spatially correlated rock-fluid interactions at all scales. Figure 1 shows long duration seismic wavetrain coda waves of hectohertz (hHz) energy. The multi-second coda wavetrains recorded at 2.5km depth arise from scattering of seismic waves emitted by Meq slip events induced at 6km depth below the sensors [1]. Some 90% of seismic wave energy emitted as ~40-80msec-duration peak P- and S-wave Meq wavelets at 6km depth has been scattered/delayed into 4-second duration coda waves during the 1-second travel time that Meq emissions take to reach the 2.5km deep sensors. The material nature of the scattering process that expands seismic emission wave energy duration by a factor 50-100 is expressed by the red hyperbolic curve $H(t) \sim 1/(a+bt)^{1/b}$. Key to our materials/methodology is that hyperbolic curves describe the drainage timeline of crustal reservoir production wells [2]. We thus ground our seismic wave discussion in the fundamental empirics relating crustal Meqs and seismic scattering to spatial distributions within reservoir fluid flow systems.

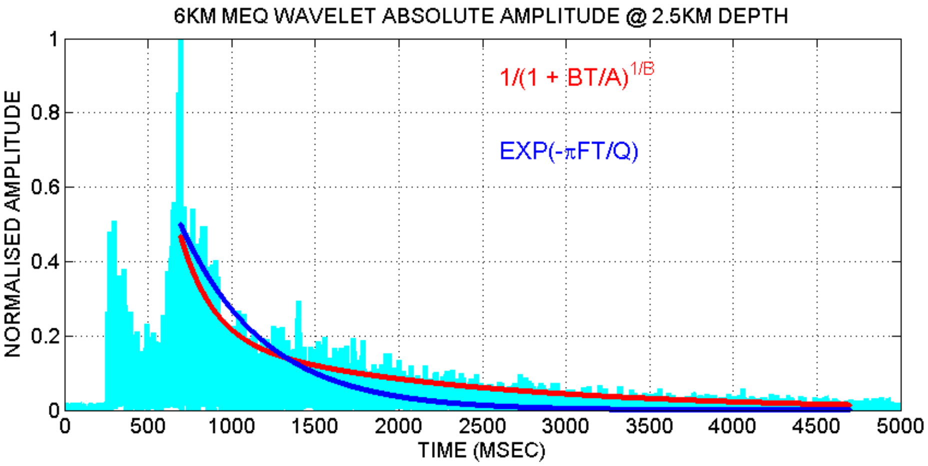

**Figure 1: Wavefield amplitude distribution for hectohertz (hHz) seismic emission at 6km depth recorded by borehole sensors at 2.5km depth directly above the event [1]. The induced Meq event wavelet (hHz frequencies f ~ 500 ± 200 Hz) given by ~ 40-80msec pulse interval at source peak S-wave amplitude at 750msec is delayed by scattering into a 4-sec interval marked by the red curve. The red coda wavetrain profile is given by hyperbolic function $H(t) \sim 1/(1+bt/a)^{1/b}$ for $b \sim 1.4$. Standard crustal coda decay curve $E(t) \sim \exp(-\pi ft/Q)$ in blue does not capture the steep decline at early times and the prolonged decline at late times. At sensor distance 4km from the Meq emission, ~90% of hHz wave amplitude is delayed**

**by scattering. The decahertz frequency data typically provided by surface sensors do not properly represent the physics underlying Meq fluid flow stimulation and induced hHz seismic wave emissions.**

Meq emission waveform spectra in Figure 2 show that little of the Figure 1 coda wave energy is lost to intrinsic anelasticity. Accordingly, the observed Figure 1 coda decline is due exclusively to energy-conserving wave scattering at ambient crust heterogeneity distributions that give rise to hyperbolic amplitude decline profiles $H(t) \sim 1/(a+bt)^{1/b}$ for oil field reservoir production well declines for parameter $b \sim ½$ [2]. Exponential decline $E(t) \sim \exp(-t/a)$ [3] in blue corresponds to hyperbolic decline parameter $b \sim 0$ and accordingly fails to describe the Figure 1 coda wave amplitude profile.

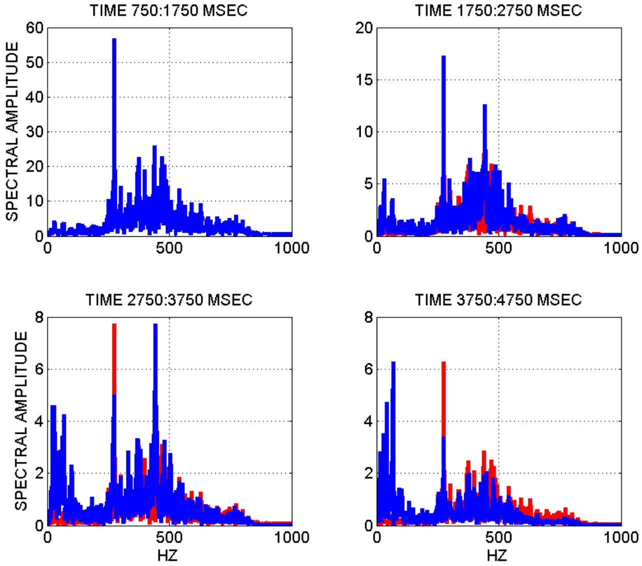

**Figure 2: Spectral amplitude distributions for Figure 1 hHz coda wavefield divided into four 1-second intervals. Spectral plots 2-4 show later interval spectra in blue superposed on the normalised initial interval spectrum rendered in red. Only in the 4th-second interval do the scattered waves begin to show wave amplitude loss relative to the initial wave; hHz wave spectral loss over 4-second travel paths is consistent with intrinsic Q ~ 3000 in accord with 2.5km deep sensor data for natural Meqs in southern California [4-5].**

In reference to standard approximations for coda wave amplitude profiles, exponential declines $E/(dE/dt) \sim -a$ are fixed in time while hyperbolic declines $H/(dH/dt) \sim -bt$ slow with advancing time given by decline rate parameter $b > 0$. Our methodological point is that hyperbolic coda declines imply the existence of delayed Meq seismic wave energy for indefinitely long periods of time after source Meq emission pulses have passed standard reservoir observation sensors. The standard expectation of exponential declines is consistent with assuming little or no delayed wave energy.

With regard to standard Meq data sets, hectohertz (hHz) scattering/delay of Meq seismic emission wave energy decisively evident in Figure 1 for deep sensors is not decisively evident in decahertz (daHz) data recorded by standard crustal reservoir surface sensors. Further, daHz Meq seismic data have not identified the strong spatial correlation systematics that link crustal reservoir Meqs with the poroperm spatial distributions that plausibly control the seismic wave scattering properties of the ambient crust indicted by Figure 1 hyperbolic decline curves $H(t) \sim 1/(a+bt)^{1/b}$. Figure 1 hHz scattering energy delay thus prompts a discussion of how processing the delayed seismic wave energy can be used to reliably locate flow-structure-related Meq emission sites as demonstrated by surface seismic array imaging currently performed at shale stimulation production sites [6-10].

As cited above, the standard treatment of reservoir Meq emissions is downloaded from fault zone seismology [11-19]. The standard treatment tacitly assumes spatially uncorrelated fracture heterogeneity in the ambient crust that is loosely associated with cubic-law fluid flow structures and seismic dislocation slip on essentially smooth planar fracture surfaces. In §§3.2-3.4 we see how Figure 1 Meq coda wave data are evidence for a specific type of spatially correlated ambient crust heterogeneity (power-law scaling "pink noise") that controls (i) rock-fluid interactions, (ii) Meq dislocation slip emissions and spatial distributions, and (iii) seismic wave scattering. With the Figure 1 seismic emission wave feature being inherent in the ambient crust and hence present in all crustal reservoirs, §§4.1-4.2 outline how Figure 1 seismic coda wave energy delay can allow mapping of active crustal flow structures via processing surface seismic array data as performed on surface array seismic monitoring data recorded at shale formation production sites.

## 3. HHZ FREQUENCY SEISMIC WAVE INTERATION WITH CRUSTAL POROPERM SPATIAL CORRELATIONS

### 3.1 Crustal reservoir Meqs -- The standard account

Fault-zone seismology conducted at slip structure scale lengths $\ell > 100$ meters has been standardised as relatively smooth rapid slip on planar dislocation surfaces [11]. Crustal heterogeneity is assumed to be spatially uncorrelated so that spatial variations are expected to average out over a sufficient number of observations. Fault-zone slip dislocation rupture speeds $v_{slip}$ are assumed to be rapid (order of shear-wave velocity $v_{slip} \sim V_S$) and quasi-uniform so that seismic wave interference internal to slip structures of dimension $\ell$ suppresses far-field seismic wave radiation above frequencies $f_0 \sim v_{slip}/\ell$. Accordingly, a conceptual seismic emission wavelet is constrained to have a constant displacement amplitude at frequencies below $f_0$ -- $A(f) \sim A_0$ @ $f < f_0$ -- with power-law declining amplitudes above $f_0$ -- $A(f) \sim A_0(f_0/f)^n$ @ $f > f_0$ for exponents $\sim 2 < n < \sim 3$. In the absence of crustal scattering, 3D seismic emission wavelets A(f) will propagate without significant modification other than amplitude loss to increasing radial expansion r and anelastic energy absorption given by $\exp(-\pi f r/V_S Q_{abs})$ in terms of quality factor $Q_{abs}$ [3].

To include seismic wave scattering in this fault-slip description of crustal Meq seismic wave propagation, it is standard to suppose that the heat absorption process given by $Q_{abs}$ is augmented by scattering as a parallel energy loss process, giving $1/Q \sim 1/Q_{abs} + 1/Q_{scat}$ [12]. This implementation of primary wavelet energy decline due to scattering focuses on the propagating wavelet without giving an explicit account of the actual scattering process. Focus on the primary wavelet thus ignores the physical fact that wave scattering such as illustrated in Figure 1 actually conserves energy and embeds the scattering systematics in the scattered wavefield.

Standard crustal reservoir Meq treatments derived from fault-zone seismology typically afford no formal recognition of scattered/delayed seismic wave energy [13-19]. For interpreting crustal reservoir Meqs, this deficiency is both omission and commission. By omission, it fails to let the full frequency and depth range of observational data dictate the physics of ambient crust Meqs emission and scattering. By commission, it enforces the simplicity of uncorrelated heterogeneity in the ambient crust conceptually stylised by Hubbert [20-21] and fed into numerical computations by, e.g., Warren [22-23], Bear [24] and Preuss [25]. While the reductive treatment of fault zone processes and fault zone seismicity is justified by a level of spatial and temporal complexity beyond our observational resources, the same is emphatically not true of the ambient crust hosted reservoir flow systems. The next sections build on crustal rock-fluid interaction empirics that define the essentially universal spatial correlation properties of the ambient crust and allow specific numerical computations to detail how ambient crust empirics affect the reservoir Meq emission waveforms illustrated in Figure 1.

### 3.2 Ambient crust fluid-rock interaction spatial correlations -- Complications for crustal reservoir Meqs

Vast reservoirs of well-log, well-core, and well-flow data attest the spatial correlation nature of rock-fluid interactions in the ambient crust [26-34]. The specifics of these essentially universal ambient crustal empirics are:

- Well-log sequences of fluid-related crustal physical properties -- porosity, sonic velocity, gamma ray emitting chemical abundances, electrical conductivity -- have power-law scaling Fourier power-spectra $S(k) \sim 1/k^{\beta}$, $\beta \sim 1$, across the spatial frequency range 1/km < k < 1/cm [26-27]; the $\beta \sim 1$ scaling form of random fluctuations is known as "1/f noise" or "pink noise" in contrast with alternative power-law scaling spectral distributions $\beta \sim 0$ (i.e., white noise) and $\beta \sim 2$ (i.e., red noise).

- Well-core sequences of porosity $\varphi$ and permeability $\kappa$ are spatially correlated as $\delta\varphi \sim \delta\log\kappa$ from core-scale to reservoir scale [28-29].

- The integrated poroperm correlation relation $\kappa(x,y,z) \sim \exp(\alpha\varphi(x,y,z))$ obeys the constraint $\sim 3 < \alpha\underline{\varphi} < \sim 5$ for formation mean porosities $\underline{\varphi}$, guaranteeing lognormal well-flow-scale distributions $\kappa(x,y,z)$ as observed for all crustal fluids [30-31].

Accompanying these fluid-rock interaction empirics are associated Meq empirics:

- Meq locations are spatially correlated via the 2-point power-law scaling function $\Gamma(r) \sim 1/r^{1/2}$, which is statistically congruent with the spatial distribution of crustal permeability $\kappa(x,y,z)$ [32-33].

- Meq magnitudes are not Gutenberg-Richter fractally distributed as in fault zones but rather are lognormally distributed in line with crustal permeability [34].

- Meq emission wavelet spectral distributions are consistent with slow erratic dislocation slip velocities and inconsistent with rapid smooth dislocation slip velocities [35-38].

The power-law-scaling spatial correlation nature of porosity and associated fracture/flow properties have a direct and pervasive impact on crustal scattering. In contrast to standard crustal scattering treatments based on a single scale length [39], scattering at spatially random wave speed velocity fluctuations in the ambient crust must be seen as systematically occurring over decades of scale length, from random spatial fluctuations smaller than the shortest wavelengths to random spatial fluctuations larger than the longest wavelengths. It is immediately apparent that no form of spatial averaging of crustal seismic wave scattering events will provide a satisfactory framework with which to address the operational problems posed by reservoir spatial flow heterogeneity. As spatial correlation heterogeneity scales with spatial dimension, the largest magnitude variations in both wave scattering and flow-structure fluctuation occur at the reservoir scale. Sampling spatial fluctuations at smaller scales – e.g., well logs and well core -- does not define flow structures at larger scales. Further, power-law-scaling spatially correlated flow structures do not guarantee that large scatters or large seismic emitters are spatially associated with the most significant reservoir flow-connectivity structures. What we can expect, and prepare to benefit from, these empirics is that significant reservoir flow structures are sources of persistent flow-related Meq emissions that can be detected if we comprehend the relation of ambient crust Meq emissions to fluid flow structures.

Given the power-law scaling spatial complexity of ambient crustal flow structures, we consider how to involve crustal reservoir Meq emissions across the full range of energy scales rather than, as hitherto, focusing on isolated Meqs. Large isolated Meq wave emission site do not necessarily contain spatial information relevant to the erratic crustal flow structures that define the main structure of convective reservoir flow, nor at such events particularly well located by standard seismic velocity models. We further note that perhaps 90% of crustal reservoir Meq wave energy occurs in surface seismic sensor data as delayed background. We therefore systematically study crustal reservoir background seismic emission energy spread over seconds as fundamentally more important than foreground energy of a few tenths of a second duration.

### 3.3 Physical origin of Figure 1 hyperbolic decay distribution of seismic scattering coda

The rate at which wavefront energy is scattered in Figure 1 is set by the hyperbolic curve parameter b in $H(t) \sim 1/(a+bt)^{1/b}$. As $b \rightarrow 0$, the expression approaches the exponential function; i.e., for $n = 1/b$, $\lim_{n\rightarrow\infty} 1/(1+x/n)^n \equiv e^{-x}$ for $x = t/a$. The case of exponential decay can thus be formally seen as a statement of no scattering, with a propagating wavefront amplitude declining due only to geometric attenuation and possible intrinsic energy lost to anelastic deformation [3]. In the presence of energy-conserving scattering, the larger the value of b the more quickly scattering generates coda waves by depleting the propagating wavefront.

We now follow [2] in formally casting the Figure 1 hyperbolic formalism as a statement of crustal power-law-scaling spatial correlation -- i.e., show that seismic wave scattering in the crust is physically related to the above ambient crust poroperm spatial correlation empirics. We then replicate crustal scattering by simulating acoustic wave scattering for power-law scaling spatially correlated random noise distributions of acoustic wave velocity. These simulations shows that Figure 1 hyperbolic decline curve parameter $b \sim 1.4$ is due to "pink noise" scattering distributions characteristic of the ambient crust. In contrast, "white noise" and "red noise" scattering distributions generate hyperbolic declines with $b \sim 1$.

Hyperbolic decline curves in oil field well production have been recognised for 100 years. Well production data P(t) fix the decline curve condition $d(P/(dP/dt))/dt \sim - b$ for $b > 0$ a constant for a given production field. This condition says that ratio of well production P(t) to rate of production dP(t)/dt falls at a constant rate given by the parameter b. Integrating well production decline gives $P/dP/dt \sim -bt + a$, 'a' an integration constant fixed by the initial production in ratio to production rate. A second integration makes explicit the slowing down of production rate $dP/P \sim -dt/(a + bt)$, whence we see that production is a power-law in time, $\log(P) \sim -b \log(a+bt)$, leading to $P(t) \sim (a + bt)^{--1/b}$ as given in Figure 1.

The contrasting Figure 1 exponential curve $P(t) \sim \exp(-t/a)$ derives from the estimated well production analysis condition $P/(dP/dt) \sim -a$, in which the rate of production decline dP(t)/dt is a fixed fraction of the current production, $dP/dt \sim -1/a\ P(t)$, leading to the exponential form. While 100 years ago it was not recognised that hyperbolic declines were implicitly scale-free power-law distribution as seen in well-log, well-core, and well-production empirics, today we can make this association, and hence can physically connect ambient crustal flow fabric with seismic wavefield scattering in Figure 1.

### 3.4 Numerical acoustic wave scattering in spatially-correlated permeability structures $\kappa(x,y,z) \sim \exp(\alpha\varphi(x,y,z))$

We expand our interpretation of Figure 1 coda wave scattering by numerically simulating acoustic scattering for crustal media embedded with power-law scaling random noise distributions derived from well-log, well-core, and well-flow empirics. Figures 3-6 illustrate how crustal parameters define the acoustic model coda profile by fixing the degree of spatial correlation of the velocity fluctuations through the Fourier spectral power scaling condition $S(k) \sim 1/k^{\beta}$, $0 < \beta < 2$, over 9 octaves of scale length. The observed ambient crust spectral fluctuation power scaling exponent has value $\beta \sim 1$, a form of spatially correlated spatial fluctuations colloquially known as "pink noise". Related random physical fluctuation distributions are given by exponent values $\beta \sim 0$ and $\beta \sim 2$; $\beta \sim 0$ with a constant/flat spectral distribution similar to white light (all frequencies having equal power) leads to the colloquial term "white noise", while $\beta \sim 2$ with low frequency power strongly pronounced over high frequency power arising from sharp interfaces is termed "red noise". Figure 4 left to right 2D sections visually distinguish white, pink, and red noises respectively.

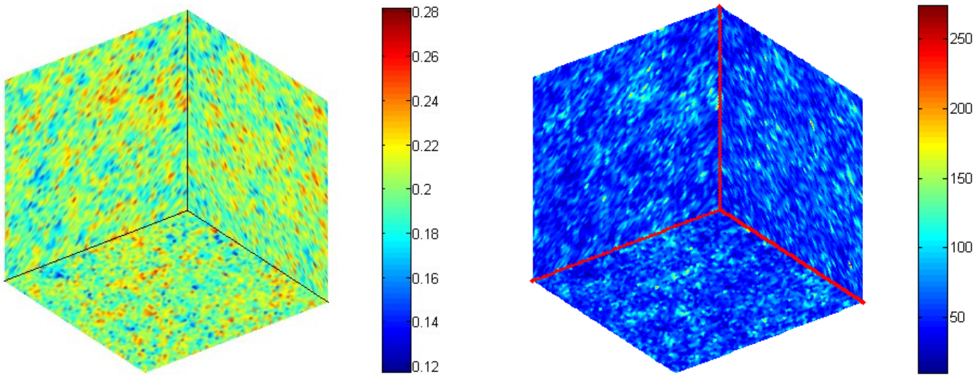

**Figure 3: (Left) Numerical realisation of spatially-correlated 3D porosity distribution $\varphi(x,y,z)$; the spatial correlation is such that logging a wellbore through the porosity field will record spatial fluctuations $\varphi(s)$ such that the Fourier spectral power scales inversely with spatial frequency k, $S_{\varphi}(k) \sim 1/k^{\beta}$, $\beta \sim 1$. (Right) The associated permeability field $\kappa(x,y,z) \sim \exp(\alpha\varphi(x,y,z))$ for $\alpha = 20$ in arbitrary permeability units.**

Figures 3-4 make an essential point that, while the conceptually unbounded power-law scaling ambient crust rock-fluid interaction properties are difficult to represent mathematically (all the more in 3D), it is straightforward to numerically represent these properties in 3D cubes or 2D sections.

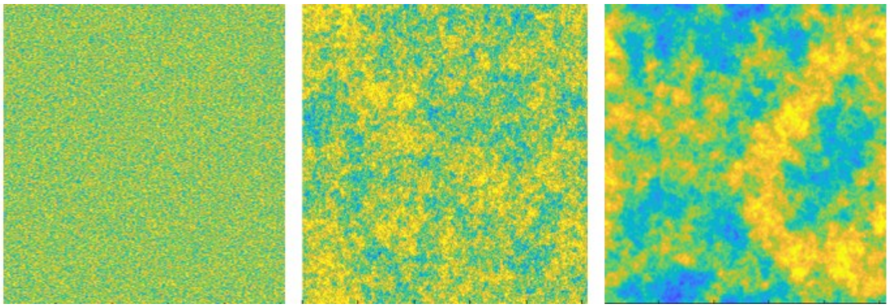

**Figure 4: 2D acoustic velocity sections showing increasing degrees of spatial correlation. (Left) White noise = minimum correlation; (Mid) pink noise = median correlation; (Right) red noise = maximum correlation. The respective 3D noise volumes are constructed so that a well-log sequence across any section obeys the following Fourier power-spectral scaling conditions: $|A(k)|^2 \sim 1/k^\beta$, $\beta = 0$, $\beta = 1$, $\beta = 2$, for nine octaves of spatial frequency $1/512 < k < 1$. While both the white noise and red noise spatial correlations are routinely applied to the ambient crust, only the §3.2 pink noise spatial correlation condition is actually observed in the ambient crust. White spatial noise is uncorrelated while red noise randomness approximates sharpish interfaces for porosity variations in successive geological formations.**

In addition to ambient crust spatial correlations controlled by well-log power-law spectral scaling $0 < \beta < 2$, well-core porosity and permeability spatial fluctuations are statistically correlated by the relation $\delta\varphi \sim \delta\log\kappa$ observed over two decades of porosity range, $0.05 < \varphi < 0.3$ for reservoir formations and $0.003 < \varphi < 0.01$ for crystalline basement. A third ambient crust rock-fluid interaction empiric is the integrated form of the well-core empiric $\kappa(x,y,z) \sim \exp(\alpha\varphi(x,y,z))$ attested worldwide as lognormal distributions of well-flow in crustal formation enforced by constraint empiric $\sim 3 < \alpha\underline{\varphi} < \sim 5$ across the range of formation mean porosities $0.003 < \underline{\varphi} < 0.3$. The value $\alpha = 20$ for Figures 3-4 is standard for the ambient crust.

Taking the Figure 3 porosity data cube to represent a volume of ambient crust, we may take the pictured spatially correlated fluctuations as occurring in seismic or acoustic velocity rather than in porosity (e.g., as an instance of Wyllie's law $1/v = \phi/v_f + (1-\phi)/v_r$ for porous media with compressive velocity v varying with porosity $\phi$ for mean compressive velocities of fluid $v_f$ and imporous rock $v_r$). As a computational simplification, we may further suppose an acoustic rather than an elastic medium with an acoustic pressure pulse source at its center. The source wavelet propagates outward to the data cube edges. Pressure wave compressions/rarefications encountering a material inhomogeneity generate scattered wave compressions/rarefications in the wake of the outwardly expanding wavelet. The Figure 5 pressure wavefields in the interior of each figure are numerical realisations of the Figure 1 coda wave amplitude profiles. The essential coda wave parameter is the degree of spatial correlation of the velocity spatial fluctuations. Conceptually, the scope and range of physical properties embodied in white, pink, and red spatial noise distributions lie completely outside standard scattering formulations [39].

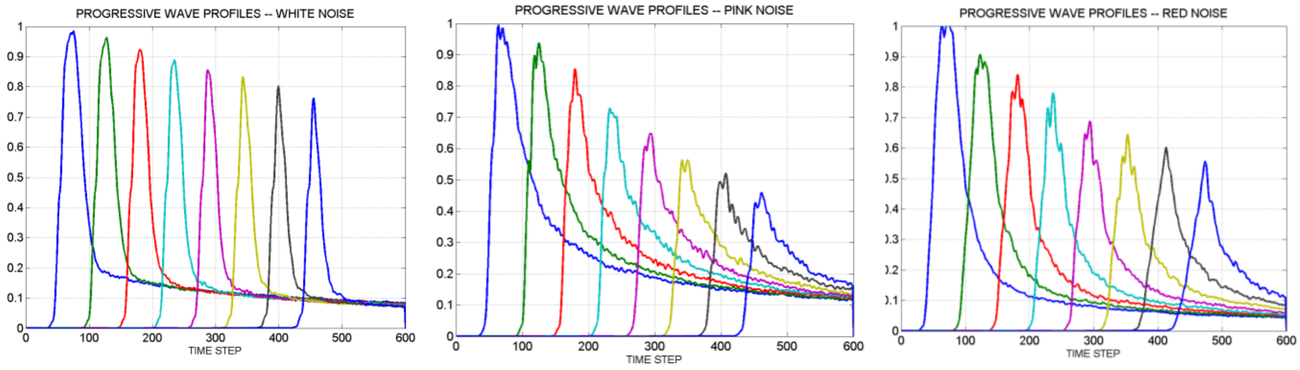

**Figure 5: (Left to right) Progression of normalised numerical wavetrain profiles at successive source-sensor offsets for white, pink and red noise distributions respectively. As illustrated in Figure 1, long-range coda profiles show that scattered wave energy radial distribution in the crustal volume accord with the class of hyperbolic functions $H(t) \sim 1/(a+bt)^{1/b}$, $0 < b < 2$. Pink noise retains higher scattered energy for longer periods of time than do white noise and red noises of equal fluctuation amplitude.**

Differences in Figure 5 waveform profile progression are due to the spatial correlation nature of the medium. In each case, the waveform peak amplitude declines due to geometric spreading. Pink noise is seen to induce a higher level of long-term persistent scattered redistribution of wavefront amplitude than either white or red noise. Numerical methods are not able to accurately propagate wavelets for arbitrary waveform travel distances, but Figure 5 scattering simulations establish the Figure 6 essential propagation trends for hyperbolic curve $H(t) = c/(a+bt)^{1/b}$ analysis.

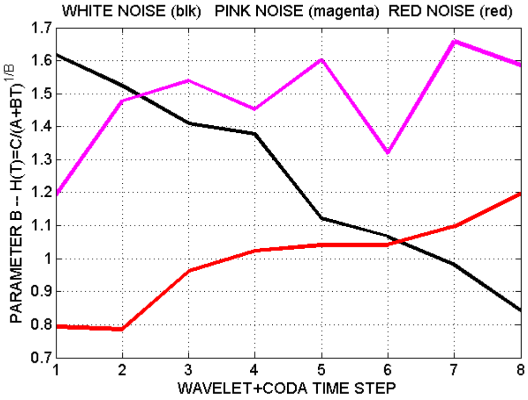

**Figure 6: Hyperbolic curve $H(t) = c/(a+bt)^{1/b}$ fit parameter b values for amplitude profiles of progressive numerical wavelet + coda scattering profiles given in Figure 5. White noise (blk) systematically declines due to averaging over uncorrelated scattering heterogeneity. Scattering by red noise is systematically smaller than scattering by pink noise.**

Figure 6 model values of the hyperbolic decline curve $H(t) = c/(a+bt)^{1/b}$ parameter b establish the respective trends for scattering wavefields in white, pink, and red noise distributions. Referring to Figure 4 white, pink, and red random structure displays, we expect to find a steady downward trend in parameter b for white noise; uncorrelated structureless randomness is subject to the standard signal/noise ratio increase $S/N \sim \sqrt{n}$ with increasing number of observations n. That is, the greater the scattering wavefield travel path, the more the wavefield is subject to uncorrelated disorganised wave interference to remove the effects of wavefield structure. Pink and red scattering noises have structured randomness which favour the preservation of longer wavelengths that undergo fewer scattering incidents per travel time duration, thus extending the coda. We see in Figure 6, however, that the Figure 4 incidental quasi-interface structures of red noise are less effective than the more diffuse scattering of pink noise in extending the coda wavefield. The Figure 6 white-pink-red spatial correlation noise phenomenon is similar to that seen in two-point spatial correlation functions $\Gamma(r) \sim 1/r^p$ exponents. For white and red noise flow structure spatial correlations are weaker -- exponent $p < \sim 0.5$ -- than for pink noise correlations -- $p \sim 1$ [10]. Detailed application of hyperbolic curves to model scattering coda amplitude profiles shows that spatial correlation systematics at work in crustal flow structures are also at work in crustal scattering structures.

## 4. APPLYING HYPERBOLIC SCATTERING FORMALISM TO AMBIENT CRUST HHZ MEQ EMISSIONS

### 4.1 Meq ~ Permeability nexus and high frequency scattering coda energy delay in the ambient crust

We now set Figure 1 ambient crust seismic wave scattering directly into the context of managing crustal reservoir flow complexity illustrated by Figure 7. Evaluating Darcy's law for Figure 3 permeability structures visually expresses the large-scale flow channelisation characteristic of crust reservoirs. With porosity spatially correlated at all scales (i.e., porosity spatial fluctuations obey the §3.2 ~ 1/k empirical spectral scaling relation), connectivity between pores is also spatially correlated. If porosity is expressed as a numerical density n, the ability of pores to link into larger scale permeability structures is proportional to the combinatorial factor $n! = n(n-1)(n-2)\ldots\ldots$ Spatial fluctuations in pore-density $\delta n$ thus create changes in pore-connectivity $\delta\log(n!)$, giving a physical interpretation to the well-core empiric by application of Stirling's formula: $\log(n!) \sim n\log(n)$ by which $\delta\log(n!) \sim \delta n$ recovers the well-core empiric $\delta\varphi \sim \delta\log(\kappa)$.

The immediate effect of Figure 7 flow channelisation on well-flow distributions is easily seen. In line with lognormal well productivity distributions everywhere, most wells intersecting the Figure 7 flow section are poor producers relative to production to be had from the few wells that intersect the high flow channels. Given that zones of higher porosity are empirically more pore-interconnected and are manifestly weaker, fluid-induced Meqs are logically most likely to occur at sites where injected fluid pressure is most active. We thus establish a Meq ~ Permeability nexus [38] with the logical consequence that detecting seismic emissions from the most active stochastic flow-connectivity structures in crustal volumes can guide production well drill bits to the main flow structures within a reservoir volume.

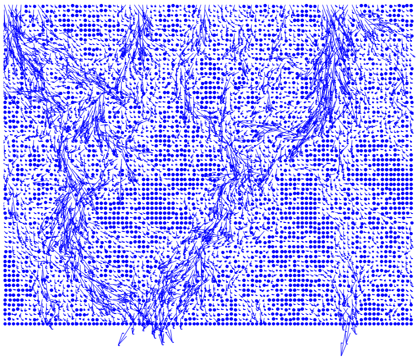

**Figure 7: Illustration of fluid flow stochastic spatial complexity in a 2D section of the Figure 3 volumetric permeability distribution $\kappa(x,y,z) \sim \exp(\alpha\varphi(x,y,z))$ for $\alpha \sim 20$ and mean porosity $\underline{\varphi}$ ~ 0 2. If flow-related seismic emissions can be detected by surface sensor arrays and processed into emission maps, it becomes possible to track such stochastically erratic flow channels to enable targeted drilling of crustal reservoirs.**

Figures 8-9 deepen the spatial relation between crustal fluid flow and crustal seismicity. There is statistical congruence between spatial distributions of ambient crust stochastic flow structures in Figure 7 and the spatial distributions of seismic slip events in the ambient crust. Figure 8 (left) shows the spatial distribution of a section of Figure 3 permeability 'events', i.e., the spatial distribution of higher density stochastic porosity that generate clusters of higher density permeability/connectivity. The power-law scaling two-point spatial correlation structure of the permeability event distribution $\Gamma(r) \sim 1/r^{1/2}$ is displayed in Figure 9 (right).

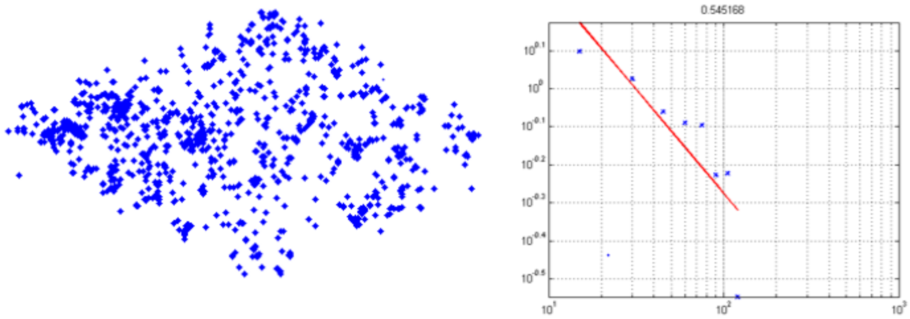

**Figure 8: (Left) Spatial distribution of high-permeability sites for a slice through the Figure 3 numerical permeability field. (Right) Two-point spatial correlation function of left-hand sites of high seismic slip potential; the observed slope on the loglog plot corresponds to the function $\Gamma(r) \sim 1/r^{1/2}$ over a decade range of site-offset.**

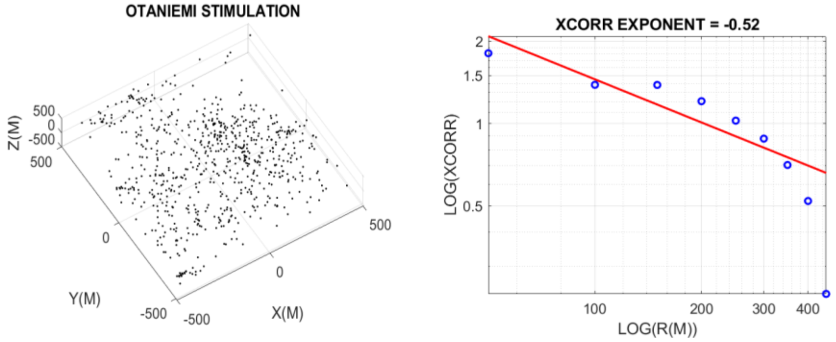

**Figure 9: (Left) Spatial distribution of microseismic events stimulated by fluid injected at 6km depth in basement rock [1]. (Right) The two-point spatial correlation distribution approximates the function $\Gamma(r) \sim 1/r^{1/2}$ over spatial offset range 50-400 meters. The Meq spatial correlation is consistent with the two-point spatial correlation registered for numerical realisations of crustal permeability distributions as visualised in Figure 3 and its flow channelisation in Figure 7.**

The high permeability sites in Figure 8 are logically sites that will slip when injected with fluids. High permeability sites are subject to entry by injected high pressure fluids. The associated high porosities make these sites locally weak and subject to dislocation slip.

Figure 9 bears out the logical expectation that ambient crust microseismicity events are spatially correlated as $\Gamma(r) \sim 1/r^{1/2}$ in line with Figure 8 high permeability "events".

The Meq events of Figure 9 (and Figures 1-2 also) are the product of sustained/controlled fluid injection in the geological setting of [1]. Figure 10 further deepens the Meq ~ Permeability nexus in terms of the observed hHz spectral systematics of the stimulation Meq emission events recorded at 2.5km depth above the stimulation volume. Rather than observing waveform spectra in the daHz range $10\text{Hz} < f < 100\text{Hz}$ expected for standard rapid Meq dislocation slip along planar fracture surfaces (given as red traces), the observed Meq emission waveform spectra (given as black traces) are centred three octaves higher in the hHz range $300\text{Hz} < f < 700\text{Hz}$. Following the work of Haskell on elastodynamic seismic radiation [35-37], the observed Meq spectra can be modelled as arising from slow erratic dislocation slip within weak pink noise spatial distributions of high-porosity/high-permeability rock associated with the Figure 3 crustal poroperm empiric $\kappa(x,y,z) \sim \exp(\alpha\varphi(x,y,z))$ [38].

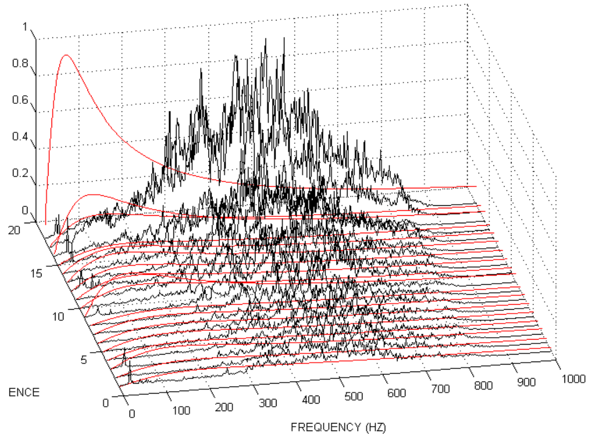

**Figure 10: Deep crustal stimulation Meq high frequency waveform spectra in black [1] compared with standard spectra distributions in red expected from dislocation planar slip emissions for Meq magnitudes $-1 < m < 1$ assigned to the events [11,13-19]. Observed hHz Meq emission spectra are attributable to slow erratic dislocation slip on reactivated permeability structures rather than rapid slip along fault-like planar structures [38].**

The observed Figure 10 high frequency Meq slip emissions give rise to the scattering transfer of seismic wave energy from the emission wavefront to the trailing coda wave. In line with Figure 1 scattering coda and the Figure 2 Meq spectral distributions, Figure 11 gives further field seismic evidence to illustrate the characteristic effects of crustal scattering on hHz seismic emission waves. The red trace coda profiles given as hyperbolic curves $H(t) = c/(a+bt)^{1/b}$ link ambient crust seismic wave scattering to the empirics of ambient crust spatially collected poroperm distributions.

The hyperbolic function scattering systematics applied to 20 Meq events of the Figure 9 spatial distribution are shown in Figure 12., Each of the 20 event wavefields recorded at 2.5km depth. e.g., Figures 1 and 11, are fit to the hyperbolic coda wave amplitude decline curves $H(t) = c/(a+bt)^{1/b}$ for a duration 4 seconds. Figure 12 displays the sequence of field data fit parameters a,b,c as black dots seen in 3D view. The black dot distribution of field data parameters is one of several numerical model synthetic wavefields given by red circles denoting hyperbolic curve fit parameter values. The sequence of red circle parameter fits to field data correspond to the Figure 5 progression of model sensor offset wavefields for pink noise scattering. Later sensor offset wavefields with more developed coda fit the field data better than earlier wavefields.

The range of model wavefield parameters corresponds to the range of field wavefield parameters, indicating the robustness of the hyperbolic curve formalism in describing ambient crust scattering coda formation and Meq wavefield energy distribution. These results are physically grounded evidence that seismic wave scattering in the ambient crust systematically redistributes seismic wave energy from the emission wavelet of duration $\tau \sim 50\text{-}100$ msec to wavefield coda of duration $\tau \sim 4000$ msec. Surface seismic sensor arrays are thus in principle sensitive to reservoir seismic emission energy detection for periods of order of seconds after reservoir Meq emissions. In the next section we model the multi-channel seismic signal stacking process that realises this principle.

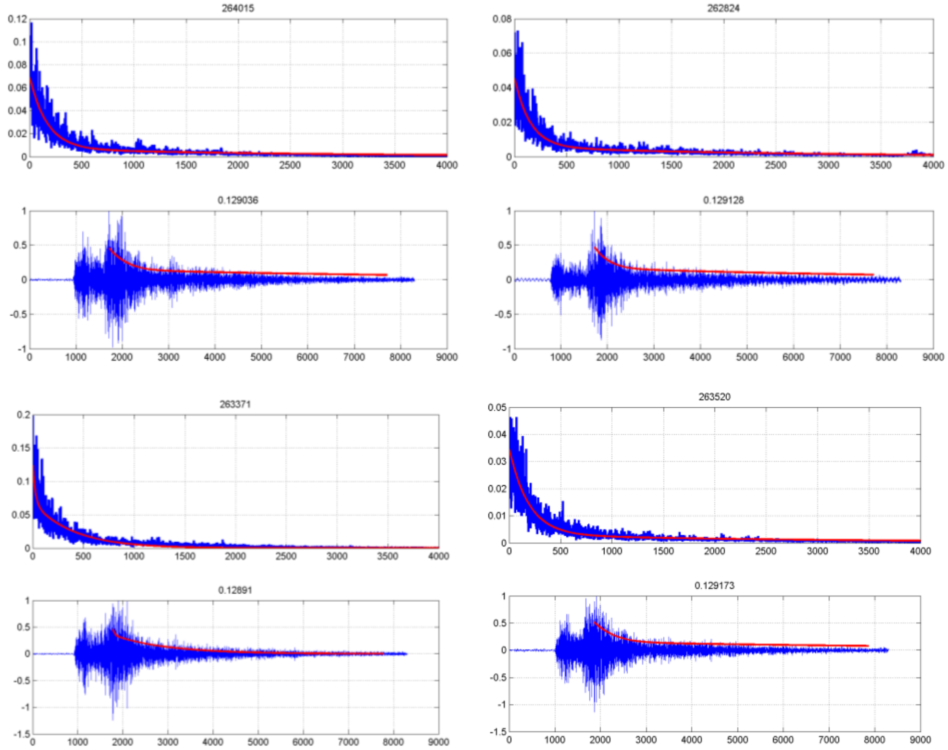

**Figure 11: Sample quartet of Figure 8 stimulation Meq events recorded over a 20-hour interval. Lower panels show 7 seconds of event waveform with coda amplitude twice the rms amplitude before the P-wave arrival. Upper panels detail the coda energy fits in red over 4 seconds of S-wave coda energy profile. The hyperbolic function H(t) = c/(a+bt)$^{1/b}$ coda amplitude profile fits (red traces) are virtually identical for observed events, indicating similar scattering properties for the otherwise distinct slip events within the stimulation volume. All event waveform spectra are consistent with spectra in Figures 2 and 10.**

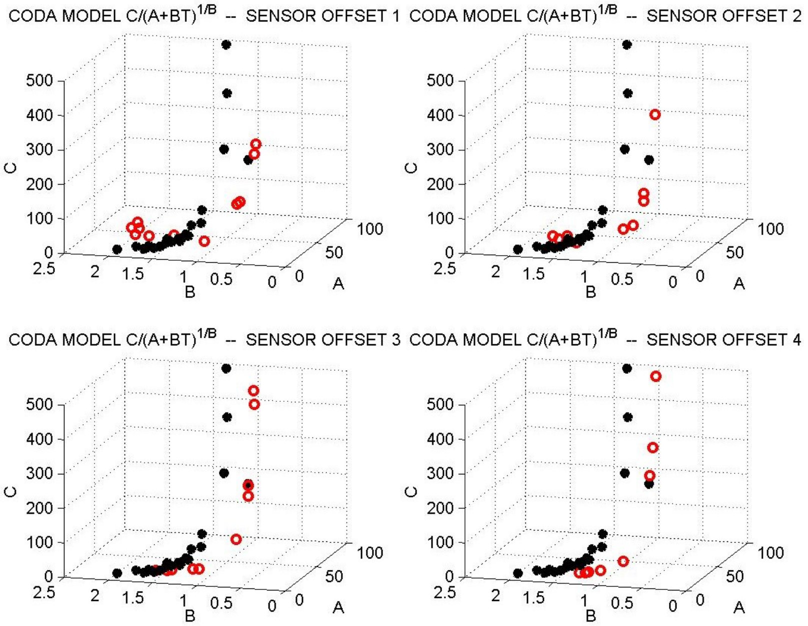

**Figure 12: View of hyperbolic function H(t) = c/(a+bt)$^{1/b}$ fit parameter a,b,c distributions for 20 observed Meq wavefields (black dots) and numerical model wavefield coda (red circles) for a sequence of model sensor offsets as seen in Figure 5. Later sensor offsets (lower right) provide better coda waveforms fits than the early offsets (upper left).**

### 4.2 Algorithmic multi-channel Meq seismic coda wave energy imaging of crustal reservoir flow structures

Standard crustal reservoir Meq seismic monitoring data are typically processed for compact high amplitude events well above background seismic activity on a number of sensor channels. The arrival time of each visible wavelet is measured for the purpose of spatially locating the event source in the manner of earthquake locations [40]. Crustal scattering spreads Meq event source wavelet energy over 50 to 100 times the duration of compact emission intervals, e.g., $\tau_{src} \sim \ell/v_{slip} \sim 50m/1m/msec \sim 50msec$ for slow slip velocity $v_{slip} \sim 1m/s$ over a rough permeability structure of dimension $\ell \sim 50$ [38]. Under scattering amplitudes of small events on surface sensor records can disappear into the background, making automated event scans ineffective. Detecting scattered event source wave energy packets requires an algorithmic procedure for scanning across multiple sensor channels using an accurate velocity model build a coherency stack of the scattered seismic wavelet energy. Such algorithmic scans for small event scattered energy signal clusters thus require a more accurate velocity model of the survey reservoir volume than is often available for reservoir volumes.

While algorithmic processing of multichannel seismic data has been investigated for decades [e.g., 41-44], we consider here only a simple direct *ab initio* 3D prescription focused on our immediate context of Figure 1 Meq source wavelet scattering coda data with a known velocity structure. A nominal $\tau_{src} \sim \ell/v_{slip} \sim 50$ msec Meq dislocation slip event wavelet of displacement velocity $\mathring{u}$ emitted at 6km depth travels 4km upwards to reach sensors at 2.5km depth in the form of a 4-second-long coda wavetrain. A quasi-plane wave of displacement velocity $\mathring{u}$ at the sensor has wave energy density $\varepsilon = \rho\mathring{u}^2$ J/m$^3$ and energy flux $\rho\mathring{u}^2 V_S$ J per unit time and unit area [45]. By conservation of energy, unscattered wavelets of emission duration $\tau_{wav} \sim 50$msec and displacement velocity $\mathring{u}_0$ expand to a scattering wavetrain of coda duration $\tau_{coda} > 4000$ msec by reducing the mean wave displacement velocity according to a condition roughly given by total emission wavelet energy at a given travel time expanded to a total coda wave energy at the same travel time, $\tau_{wav}\mathring{u}_{wav}^2 \sim \tau_{coda}\mathring{u}_{coda}^2$. Following coda production seen in Figures 1 and 11, the prospective coda wave amplitude is a factor 10 smaller than the source emission wavelet without scattering, $\mathring{u}_{coda} \sim \mathring{u}_{wav}\sqrt{(\tau_{wav}/\tau_{coda})} < \mathring{u}_{wav}/10$. The point of the algorithmic scan for flow-related Meq emission events is thus to explore surface sensor array data for coherency stacks of reduced amplitude extended-wave coda signals.

To numerically simulate the extended coda wave coherency stacking process, we model a 4km dimension crustal volume with a cubic mesh of 512 nodes per side at 8 meter nodal spacing. On the crustal surface a 25 x 25 sensor grid is centred at 16m spacing. An Meq source is arbitrarily located a depth in the volume. Following Figure 3, the crustal volume is filled with spatially correlated acoustic velocity fluctuation scattering noise with 6% rms fluctuation amplitude about the mean velocity as seen in sonic velocity well-log data worldwide. Travel times $TT_{nm}$ , n = 1:$N_{vox}$, from every potential 16x16x16 m$^3$ subsurface source voxel to each of the m = 1:$N_{sns}$ surface sensors are computed by a Matlab-implemented Fast Marching Method (FMM) algorithm [46]. With a particular voxel nominated to be the Meq emission coda wavefield source, two suites of model sensor data are constructed, one with a 50msec unscattered Meq emission wavelet, the other with a 4000msec scattered coda wavefield.

The model sensor traces in which the emission wavelet and scattered coda wavefield are embedded are band-limited uncorrelated random (Gaussian or white) noise of unit rms amplitude. The input data to be processed comprises 625 1-minute-long background sensor traces broken into 60 1-second-long sample traces. Each second-long sensor trace consists of 120000 half-msec samples in line with the field data [1]. While in principle each second-long sample of sensor data is unlikely to have an embedded Meq signal, for illustration purposes an Meq signal is embedded in each second-long sensor noise trace throughout the 60 second data set. The peak amplitude of the embedded wavelet signal is 1/3 of the unit rms noise, and the coda wave peak amplitude is 1/30 of the embedded wavelet peak amplitude. In each sensor trace, the position of the emission wavelet and the extended coda wave is given by the FMM travel-time between the sensor location and the emission source location. The computed sensor traces are then lowpass filtered to correspond to daHz data recorded by standard surface sensors.

The task of processing the model data set uses travel-time table $TT_{jk}$, j = 1:$N_{vox}$, k = 1:$N_{sns}$, to compute an $N_{sns}$-fold data stack for each 1-second time window $\tau_{win}$ for each of $N_{vox}$ potential/trial subsurface source sites. The trial source voxel site that corresponds to the selected source site will contribute travel-times that accurately reverse the time shift used to construct the sensor data. All other sets of time shifts will either under-shift or over-shift the sensor trace relative to the position of the embedded source wavelet or coda wavetrain. At the end of the sensor trace travel-time shifting operation, the resulting $N_{sns}$ time-shifted seismic wave traces are summed to give a $N_{sns}$-fold signal stack trace for each of the $N_{vox}$ voxels.

The signal stack corresponding to the selected source location is summed over traces in which the source wavelet or coda wavetrain have been aligned in time. The aligned signals will add constructively over the $N_{sns}$-fold stack. The sensor traces for all other trial source voxels will be misaligned to some degree, and the stack of misaligned wavelet/coda-wavetrain will be proportionately smaller as the misalignment grows. We then find which $N_{sns}$-fold voxel stack has the highest amplitude.

Figure 13 illustrates the result of this processing task for a representative set of 21 trial voxel stacks. Red circles show the sum of 60 1-second voxel stacks for the Meq wavelet, and red squares show the sum of 60 1-second voxel stacks for the coda wavetrain. For the chosen signal amplitudes relative to sensor noise (1/3 and 1/30 for emission wavelet and coda wavetrain respectively), the chosen number of sensors (625), and the chosen number of Meq events (1 event per second for 60 seconds), we see that both the emission wavelet and the coda wavetrain return a signal that is comfortably greater than the background sensor noise level. As expected, the compact energy distribution of the emission wavelet produces a higher signal than the extended energy distribution of the coda wavetrain, but the essential point is that Figure 1 field-mandated coda wavetrain stacking signal can be easily detected for the given stacking parameters. In the case of smaller signal/noise ratio for the model wavelets or slower event occurrence, the number of sensor data time-windows – here taken to be a nominal 1 minute of observation -- can be increased to essentially arbitrary values [6-7].

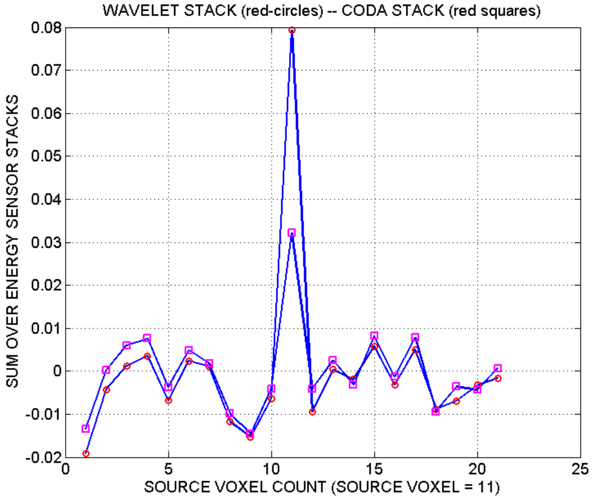

**Figure 13: Wavelet/coda coherent energy stack amplitudes for 60 time-windows for a selection of trial source voxels 1 < $N_{vox}$ < 21. The actual source voxel $N_{vox} = N_{11}$ returns a maximal value; the other trial voxels stack misaligned wavelet/coda signals, thus giving smaller signal energy estimates. The maximal energy stack value is higher for Meq wavelets than for Meq coda because wavelet energy is compact while coda energy is distributed. The point at stake is that crustal scattering of Meq wavelets that cannot be registered as individual events on surface array sensors can nonetheless be identified as energy coherency stacks across the sensor array.**

Figure 13 symbolises a large number of variations on the simple inversion scheme. Relevant processing variables include the number $N_{sns}$ and distribution of surface sensors, the number $N_{vox}$ and distribution of subsurface potential/trial source voxels, the number of time-windows $N_{win}$, the amplitude and degree of surface sensor noise complexity, the amplitude of the subsurface Meq emission relative to the surface sensor background, the accuracy of the velocity model used to compute the travel-time table, and degrees of near-surface terrain and heterogeneity correction. Moreover, the Figure 13 processing involves an event in every 1-second time-window whereas field application of this processing will have many sample time-windows with no event signal. We are, however, principally interested in self-consistent result gained by comparing the sensitivity of the inversion to the signal-type. compact emission wavelet versus distributed coda -- to assess at what level of crustal scattering does the coda wave signal fail to register a reliable inversion. Figure 19 shows that a reasonable number of surface seismic sensors (25 x 25 = 625) recording at a certain data rate (500Hz) over a certain frequency range (10-100Hz) and listening for a certain length of time (60 1-second time-windows) can build a distributed energy coda-wave detection signal comparable to a compact energy wavelet detection signal. Figure 13 illustrates the principle that crustal reservoir-flow-structure mapping facility established at shale formation production sites [6-10] can be seen in operational terms as sensitive to persistent flow-structure seismic emissions reaching the surface as distributed scattered coda wave energy that has been identified in Figure 1 field data.

## 5. CONCLUSIONS

We have introduced a suite of ambient crust Meq waveforms that (probably) for the first time demonstrates the high-frequency content of seismicity induced at reservoir depths in the ambient crust. The induced Meq emission waveform spectra in hHz frequency range f ~ 500Hz ± 200Hz are evidence for slow erratic dislocation slip on ambient crust permeability structures rather than on planar fracture structures as traditionally ascribed. Supporting the spectral evidence for slip on permeability structures, the Meq two-point spatial correlation function $\Gamma_{Meq}(r) \sim 1/r^{1/2}$ is noted to be the same as the two-point spatial correlation function for ambient crustal permeability $\Gamma_{Perm}(r) \sim 1/r^{1/2}$. In line with these two front-rank Meq spatial distribution features is our Figure 1 core observation that the hHz Meq emission wavefields are highly scattered by endemic poroperm spatial heterogeneity with the statistical properties of pink noise. Emission wavelets of plausible 50-100 msec slip duration at 6km source depth are scattered into trailing coda wavetrains of 4-second duration at the time of recording by sensors a 2.5km depth.

As standard seismic scattering formalisms fail to explain the observed Meq waveforms, we have noted that hyperbolic functions $H(t) \sim 1/(a+bt)^{1/b}$ accurately describe the induced Meq coda amplitude profiles as well as the decline profile of hydrocarbon well production. Taking P(t) to stand for either wave-pressure or fluid- production, the hyperbolic curve parameter b controls the rate of decline dP(t)/dt relative to the current value P(t) as $d(P/(dP/dt))/dt \sim -b$.

In addition to fortifying the link between ambient crustal seismic wave scattering and ambient crust fluid production, the hyperbolic curve formalism provides a convenient framework for applying numerical simulation of 3D acoustic wave scattering by which to quantify the scattering process induced by random noise poroperm distributions in the ambient crust. While numerical realisations of 3D acoustic scattering can simulate only a relatively few scattering lengths, our pressure wave scattering simulations establish coherent trends for the hyperbolic curve control parameter b. In a white noise scattering medium, parameter b grows smaller with increasing scattering wave travel as uncorrelated randomness redistributes wave amplitudes equally at all wavelengths. In pink and red noise scattering media, parameter b grows as low frequency waves scatter less often that high frequency waves. Pink noise, however, systematically scatters more efficiently than red noise, hence pink noise coda wave durations systematically exceed both white noise and red noise coda durations.

Systematising the physical origin and nature of ambient crustal scattering in terms of crustal poroperm heterogeneity makes it more straightforward to cogently deal with the considerable operational problems posed by reservoir heterogeneity as demonstrated by field-scale seismic flow structure mapping of stimulated shale formation oil and gas production. The duration of hHz seismic wave scattering in the ambient crust is of first order interest in utilising Meq emissions for better understanding ambient crustal reservoir flow structures. Scattering that extends Meq temporal distributions from wavelet durations τ ~ 50-100msec to τ ~ 4000msec indicates that some 90% of seismic emission energy exists as delayed/diffused energy registered by surface seismic sensors. While most reservoir seismic survey data processing focuses on Meq events that readily visible on most or all surface seismic data channels, crustal scattering indicates that multi-channel surface seismic sensor data processing methodologies tuned to stacking emission wavelets buried in sensor background noise can capture the order of magnitude greater detail of flow-structure information enabled by the high-frequency Meq emissions illustrated in Figures 1 and 11.

Our Figure 13 reservoir-imaging indicator is consistent with the actively realised processing of surface seismic sensor array data acquired at shale formation stimulation production sites. Multi-channel surface seismic array data from shale formation stimulation sites now routinely validate the "Meq ~ Permeability" nexus established by deep crustal stimulation Meq event spatial correlation data. The physical details of hHz Meq waveform scattering coda recorded at 2kHz by 2.5km deep sensors indicate how the Meq ~ Permeability nexus can be systematically observed via surface seismic sensor array data processed into detailed crustal reservoir permeability structure images. In the case of convective geothermal flow systems, such flow images can be used to identify sites of large and sustained convective flow for targeted drilling.

## REFERENCES

[1] Kwiatek G, Saarno T, Ader T, Bluemle F, Bohnhoff M, Chendorain M, Dresen G, Heikkinen P, Kukkonen I, Leary P, Leonhardt M, Malin P, Martínez-Garzón P, Passmore K, Passmore P, Valenzuela S & Wollin C (2019) Controlling fluid-induced seismicity during a 6.1-km-deep geothermal stimulation in Finland, Science Advances 01 May 2019: Vol. 5, no. 5, eaav7224 DOI: 10.1126/sciadv.aav7224.

[2] Arps JJ (1945) Analysis of decline curves. Trans. Am. Inst. Min. Metall. Eng. 160, 228–247.

[3] Aki K & Richards P (1980) Quantitative Seismology, §5.5, W. H. Freeman, San Francisco.

[4] Leary P & Abercrombie R (1994) Frequency dependent crustal scattering and absorption at 5–160 Hz from coda decay observed at 2.5 km Depth, *Geophysical Research Letters* 21(11):971-974b DOI:10.1029/94GL00977

[5] Leary PC (1995) The cause of frequency-dependent seismic absorption in crustal rock, Geophys. .I. Int. 122, 143-151.

[6] Geiser P, Lacazette A & Vermilye J (2012) Beyond "dots in a box", First Break 30, 63. 69.

[7] Sicking C & Malin P (2019) Fracture seismic: Mapping subsurface connectivity: Geosciences, 9, 508; 660 doi:10.3390/geosciences/120508.

[8] Malin PE, Leary PC, Cathles LM & Barton CC (2020) Observational and critical state physics descriptions of long-range flow structures, GeoSciences, 10.3390/geosciences10020050

[9] Leary P, Malin P, Saunders G & Sicking C (2020) Seismic imaging of convective geothermal flow systems to increase well productivity, Journal of Energy and Power Technology, JEPT 2(3), doi:10.21926/jept.2003012

[10] Leary P & Malin P (2021) Crustal reservoir flow simulation for long-range spatially-correlated random poroperm media, Journal of Energy and Power Technology, JEPT (3), 1, doi:10.21926/jept.2101013

[11] Aki K & Richards P (1980) Quantitative Seismology, §14.1, W. H. Freeman, San Francisco.

[12] Aki K & Chouet B (1975) Origin of coda waves: Source, attenuation, and scattering effects, Journal of Geophysical Research 80, 3322-3342.

[13] Rutledge JT, Phillips WS & Mayerhofer MJ (2004) Faulting induced by forced fluid injection and fluid flow forced by faulting: An interpretation of hydraulic-fracture microseismicity, Carthage Cotton Valley Gas Field, Texas, Bull Seis Soc Amer 94, 1817–1830

[14] Eisner L, Duncan PM, Heigl WM & Keller WR (2009) Uncertainties in passive seismic monitoring, Leading Edge, vol. 28, no. 6, pp. 648–655.

[15] James P, Verdon J, Kendall JM and Maxwell SC (2010) A comparison of passive seismic monitoring of fracture stimulation from water and CO2 injection, Geophysics 75; doi: 10.1190/1.3377789

[16] Duncan PM & Eisner L (2010) Reservoir characterization using surface microseismic monitoring, Geophysics 75, 75A139–75A146, 10.1190/1.346776

[17] Warpinski NR, Du J & Zimmer U (2012) Measurements of hydraulic-fracture-induced seismicity in gas shales, SPE Hydraulic Fracturing Technology Conference, Houston TX; SPE 151597

[18] Eisner L, Gei D, Hallo M, Opršal I & Ali MY (2013) The peak frequency of direct waves for microseismic events, Geophysics, DOI: 10.1190/geo2013-0197.1

[19] Warpinski NR (2013) Understanding hydraulic fracture growth, effectiveness, and safety through microseismic monitoring, http://dx.doi.org/10.5772/55974.

[20] Hubbert MK. Motion of ground water. Trans N Y Acad Sci. 1941; 3: 39-55.

[21] Hubbert MK. Darcy's law and the field equations of the flow of underground fluids. Int Assoc Sci Hydrol. Bull. 1957; 2: 23-59.

[22] Warren JE, Skiba FF. Macroscopic dispersion. Soc Pet Eng J. 1964; 4: 215-230.

[23] Warren JE, Root PJ. The behavior of naturally fractured reservoirs. Soc Pet Eng J. 1963; 3: 245-255.

[24] Bear J. Dynamics of fluids in porous media, New York: American Elsevier; 1972.

[25] Pruess K, Oldenburg C & Moridis G (20212) Tough2 User's Guide Version 2, LBNL-43134 Earth Sciences Division, Lawrence Berkeley National Laboratory University of California, Berkeley, California 94720.

[26] Leary PC (1997) Rock as a critical-point system and the inherent implausibility of reliable earthquake prediction. Geophys J Int. 131: 451-466.

[27] Leary PC (2002) Fractures and physical heterogeneity in crustal rock, in Heterogeneity in the Crust and Upper Mantle: Nature, Scaling, and Seismic Properties, J. A. Goff and K. Holliger, Eds., pp. 155–186, Kluwer Academic/Plenum Publishers, New York, NY, USA, 2002.

[28] Leary PC & Al-Kindy F (2002) Power-law scaling of spatially correlated porosity and log(permeability) sequences from north-central North Sea Brae oilfield well core, *Geophysical Journal International* 148, 426–442, https://doi.org/10.1046/j.1365-246x.2002.01618.x

[29] Leary P, Malin P, Saarno T, Kukkonen I (2018) $\alpha\varphi \sim \alpha\varphi_{crit}$ - Basement rock EGS as extension of reservoir rock flow processes. Proceedings 43rd Workshop on Geothermal Reservoir Engineering, Stanford University, 2018 February 12-14.

[30] Leary P, Malin P, Pogacnik J, Rugis J, Valles B & Geiser P (2014) Lognormality, dk ~ kdf, EGS, and all that, Proceedings 39th Stanford Geothermal Workshop, February 24-26 2014, Stanford University, CA.

[31] Malin P, Leary P, Shalev E, Rugis J, Valles B, Boese C, Andrews J & Geiser P (2015) Flow Lognormality and Spatial Correlation in Crustal Reservoirs: II. Where-to-Drill Guidance via Acoustic/Seismic Imaging, WGC2015, 19-24 April, Melbourne AU

[32] Leary P, Malin P, Saarno T, Heikkinen P, Diningrat W (2019) Coupling crustal seismicity to crustal permeability - Power-law spatial correlation for EGS-induced and hydrothermal seismicity. Proceedings of the 44th Workshop on Geothermal Reservoir Engineering, Stanford University, February 11-13.

[33] Leary P & Malin P (2020) Correlation function $\Gamma_{meq}(r) \sim 1/r^{1/2}$ coupling of microseismicity to permeability -- The basis for fluid flow seismic image targeting for geothermal production wells, Proceedings World Geothermal Congress 2021 Reykjavik, Iceland, 21-26 May 2021.

[34] Leary P, Malin P & T Saarno (2020) A physical basis for the Gutenberg-Richter fractal scaling, 45th Workshop on Geothermal Reservoir Engineering, Stanford University, February 10-12, SGP-TR-216 1.

[35] Haskell NA (1964) Total energy and energy spectral density of elastic wave radiation from propagating faults, Bull Seis Soc Amer 54, 118-142.

[36] Haskell NA (1966) Total energy and energy spectral density of elastic wave radiation from propagating faults, Part 2, Bull Seis Soc Amer 56, 125-140.

[37] Haskell NA (1969) Elastic displacements in the near-field of a propagating fault, Bull Seis Soc Amer 59, 865-908.

[38] Leary P & Malin P (2021) MEQ ~ Permeability. Modelling of high frequency emissions from stimulation microseismicity in the ambient crust, Proceedings World Geothermal Congress 2021 Reykjavik, Iceland,

[39] Aki K & Richards P (1980) Quantitative Seismology, §§13.2-13.3. W. H. Freeman, San Francisco.

[40] Stanek F, Anikiev D, Valenta J & Eisner L (2015) Semblance for microseismic event detection_Geophys. J. Int. 201, 1362–1369 doi: 10.1093/gji/ggv070

[41] Claerbout, JF (1971) Toward a unified theory of reflector mapping, Geophysics 36, No. 3, 467–481.

[42]_Baker T, Granat R & Clayton R.W (2005) Real-time earthquake location using Kirchhoff reconstruction. Bulletin of the Seismological Society of America, 95:699–707.

[43] Gajewski D, Anikiev D, Kashtan B, Tessmer E & Vanelle C (2007), Localization of seismic events by diffraction stacking, *SEG Technical Program Expanded Abstracts* 1287-1291; doi.org/10.1190/1.2792738

[44] Zhebel O, Gajewski D & Vanelle C (2011) Localization of seismic events in 3D media by diffraction, Third EAGE Passive Seismic Workshop - Actively Passive 2011, doi.org/10.3997/2214-4609.20145296.

[45] Aki K & Richards P (1980) Quantitative Seismology, §5.1, W. H. Freeman, San Francisco.

[46] Sethian JA & Popovici AM (1999) 3-D traveltime computation using the fast marching method, Geophysics 64, NO. 2, 516–523.